

## Research Article

# Study on the Simulation Method of the Ground Test in the Arc-Heated Wind Tunnel

Wanqing Luo<sup>1,2</sup>, Yuanjian Yang<sup>3,2</sup>, Jianhan Liang<sup>1</sup>, Songhe Zhang<sup>2</sup> and Yilei Shi<sup>2</sup>

<sup>1</sup>Science and Technology on Scramjet Laboratory, National University of Defense Technology, Changsha 410073, China

<sup>2</sup>Hypervelocity Aerodynamics Institute, China Aerodynamics Research and Development Center, Mianyang 621000, China

<sup>3</sup>School of Astronautics, Harbin Institute of Technology, Harbin 150080, China

Correspondence should be addressed to Jianhan Liang; [jhleon@vip.sina.com](mailto:jhleon@vip.sina.com)

Received 18 September 2020; Revised 31 October 2020; Accepted 13 November 2020; Published 30 November 2020

Academic Editor: Jing-Lei Xu

Copyright © 2020 Wanqing Luo et al. This is an open access article distributed under the Creative Commons Attribution License, which permits unrestricted use, distribution, and reproduction in any medium, provided the original work is properly cited.

To analyze the effectiveness of the thermal assessment test, the simulation method of the ground test in the arc-heated wind tunnel is studied. Based on the solution of the thermochemical nonequilibrium Navier-Stokes equations, the flowfield around the spherical cylinder is simulated in the flight and ground test conditions, and the difference in the high enthalpy flowfield between the flight and ground test conditions is investigated. The flight parameters and ground test conditions are selected according to the criterion that the total enthalpy and the stagnation point heat flux of the fully catalytic cold wall (calibrated heat flux) are similar. The flowfield for different temperature boundaries and different catalytic walls is solved under the same free stream conditions, and the stagnation point heat flux and oxygen atom mass fraction are compared and analyzed. It is found that the heat flux on the fully catalytic wall for the radiation balance temperature boundary in the ground test is lower than that in the corresponding flight condition, but the difference is not obvious on the noncatalytic wall. In addition, the oxygen atom mass fraction after the shock wave in the ground test is higher than that in the corresponding flight condition. To make the stagnation point heat flux and oxygen atom mass fraction after the shock wave similar to those of the flight, the simulation method of the arc-heated wind tunnel test needs to be adjusted.

## 1. Introduction

Hypersonic vehicles have received growing attention in recent years. Due to their extremely high flying speed, the kinetic energy of the free stream is converted into internal energy by shock wave compression, forming high-temperature gas with thousands or even tens of thousands of Kelvins. Gas molecules dissociate or even ionize, resulting in a strong nonequilibrium effect. These physical and chemical phenomena of hypersonic flight form large aerodynamic thermal load, acting on the aircraft surface for a long time, thus posing a severe challenge to the thermal protection material and structure of the aircraft. To achieve safe flight and successfully carry out flight tasks, the thermal protection system (TPS) must be constructed in the preliminary design. The traditional conservative design method cannot meet the increasing performance requirements, so more accurate analysis and evaluation of the aerodynamic thermal environment for aircraft is urgently needed.

The ground wind tunnel test is an irreplaceable step in aircraft development, and the arc-heated wind tunnel is indispensable for screening thermal protection material, optimizing the thermal protection structure, and guiding aircraft design [1]. However, due to the limitations of arc power and measurement method of the wind tunnel test, it is impossible to fully repeat all the parameters of the flight conditions or to obtain comprehensive data in the test flowfield by measurement. Moreover, the test cycle is long and the operating cost is high because the process is complicated, including test design, model processing, and system debugging, thus severely limiting the development progress of aircraft.

The catalytic characteristics of surface materials have a significant effect on the aerodynamic heating of nonequilibrium flow [2, 3]. In the arc-heated wind tunnel test, if the catalytic characteristic of the heat flux sensor is quite different from that of the test model, the measured heat flux will be inaccurate [4]. Generally, the total enthalpy and the

stagnation point heat flux of the fully catalytic cold wall (calibrated heat flux) are simulated in the arc-heated wind tunnel test. In other words, the total enthalpy and the calibrated heat flux are similar between the flight and ground test conditions. The water-cooled calibration model (with the model and its sensor close to fully catalytic) is usually used to calibrate and debug the flowfield in the early stage of the test. The test article without the heat flux sensor is installed in the wind tunnel for the thermal assessment test when the target flowfield parameters are obtained. Due to this simulation criterion, there are two problems in the test. First, the calibrated heat flux is based on the cold wall and fully catalytic boundary, but the surface material of aircraft is not necessarily fully catalytic, and the wall temperature is not constant for the long-time heating without water cooling in flight. Even if the calibrated heat flux between the flight and ground test conditions is rather similar, the thermal environment in the test and the real flight conditions may also be different. Second, other flowfield parameters near the model surface may also differ, such as the oxygen atom mass fraction. Its difference may lead to different oxidation degrees on the material surface between the flight and ground test conditions. In this case, the ground test cannot properly evaluate the thermal protection performance of the material or structure in flights.

Since the last century, computational fluid dynamics (CFD) has achieved great progress [5–7], becoming one of the main research tools for fluid dynamics. The high enthalpy flowfield of the flight and ground test conditions can be solved by the numerical simulation method to obtain the flowfield parameters and surface heat flux and to compare and analyze the differences between the flight and ground test conditions. The effectiveness of simulation parameters can be explored to improve the ground test simulation method and guide the ground wind tunnel test design. In addition, more comprehensive flowfield data can also be obtained through numerical simulation, which is not measured but is needed to evaluate the test environment [8]. These data are helpful to reduce the number of test debugging and the cost of test operation and shorten the development cycle of the thermal protection system of an aircraft.

The ground test techniques and high-fidelity numerical method have been combined for test planning in the arc-heated wind tunnel. Gökçen et al. [8] used the DPLR (Data Parallel Line Relaxation) program to simulate the flowfield in the axisymmetric nozzle and the flowfield around the wedge model in the test section of the arc-heated facility in NASA's Ames Research Center. The parameters such as surface pressure and heat flux of the test model were obtained and compared with the experimental data in the wind tunnel. Mark et al. [9] solved the high enthalpy flowfield in the arc-heated wind tunnel by the numerical simulation method and carried out a comparative analysis of the differences between the flight and ground conditions for X-33 and RLV (Reusable Launch Vehicle) configuration; the analysis has been used to address traceability of the ground test environment to that of flight conditions. Grinstead et al. [10] designed the test program by the numerical simulation method for a range of facility conditions to the expected aerothermal and thermochemical mechanisms of a TPS material.

It shows that numerical simulation can provide greater insight into the operating characteristics and capabilities of the arc-heated facility and optimize the test simulation method early in the planning process. In view of the influence of catalytic characteristics on the surface aerodynamic heating, Nie et al. [3] carried out the test of the spherical cylinder model in the arc-heated wind tunnel and the numerical simulation of the test flowfield. The results show that the difference between test data and numerical simulation results for the fully catalytic wall is larger than that for the noncatalytic wall.

In order to better carry out the thermal assessment test for the spherical cylinder model in the arc-heated wind tunnel, the difference of the high enthalpy flowfield between the flight and ground test conditions is investigated by the numerical simulation method. The stagnation point heat flux and mass fraction of oxygen atom distribution are compared and analyzed for the conditions with similar enthalpy and calibrated heat flux; the law of the difference between the flight and ground test conditions is obtained. And then, the test simulation method is investigated on how to simulate the surface heat flux and the mass fraction of the oxygen atom after the shock wave for the partially catalytic material.

## 2. Numerical Simulation Method

**2.1. Governing Equations.** In the three-dimensional Cartesian coordinate system, the Navier-Stokes equation is expressed as follows for nonequilibrium flow [11, 12]:

$$\frac{\partial Q}{\partial t} + \frac{\partial(E - E_v)}{\partial x} + \frac{\partial(F - F_v)}{\partial y} + \frac{\partial(G - G_v)}{\partial z} = S, \quad (1)$$

where  $Q$  is the conservation variables;  $t$  is the time; and  $E$  and  $E_v$ ,  $F$  and  $F_v$ , and  $G$  and  $G_v$  are the convection and viscous terms in three directions, respectively. The term on the right side is the nonequilibrium source term given by

$$S = [\dot{\omega}_i, 0, 0, 0, 0, \dot{\omega}_v]^T. \quad (2)$$

The internal energy of gas species includes translational, rotational, vibrational, and electronic energy. Park's two-temperature thermodynamic nonequilibrium model is used [6], in which translational energy and rotational energy are described by translational temperature, and the vibrational energy and electronic energy are described by vibrational temperature. The energy of various modes is defined based on the harmonic oscillator hypothesis, and the detailed expression is shown in Ref. [11].

For the multispecies gas mixture, the kinetic equation of chemical reaction is as follows:

$$\sum_{i=1}^{ns} \nu_{ji} A_i \xrightleftharpoons[k_{b,j}]{k_{f,j}} \sum_{i=1}^{ns} \nu_{ji}'' A_i, \quad j = 1, 2, \dots, nr, \quad (3)$$

where  $nr$  is the number of chemical reactions;  $\nu_{ji}$  and  $\nu_{ji}''$  are the chemical stoichiometric coefficients of the reactants and products, respectively;  $A_i$  is the  $i$ th chemical species

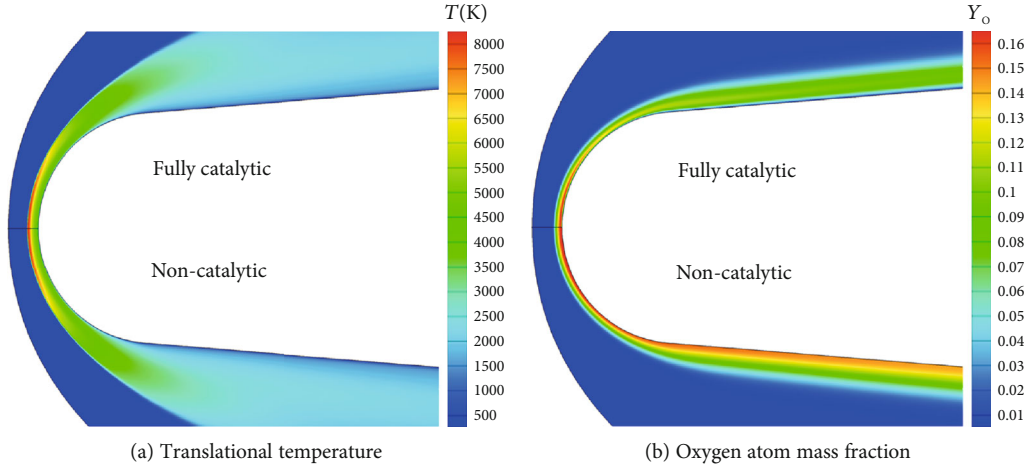


FIGURE 1: Flowfield parameters of ELECTRE.

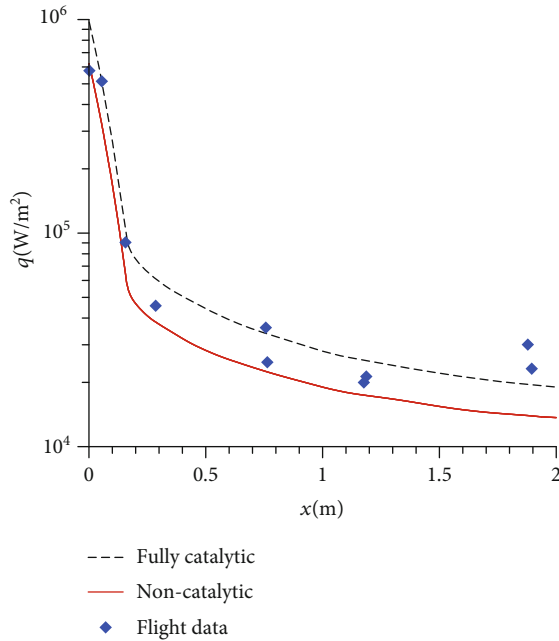


FIGURE 2: Heat flux along the surface of ELECTRE.

participating in the reaction;  $ns$  is the species number of the mixture; and  $k_{f,j}$  and  $k_{b,j}$  are the forward and backward chemical reaction rates, respectively.

The mass production of the  $i$ th species rate is given by

$$\dot{\omega}_i = W_i \sum_{j=1}^{nr} (\dot{C}_i)_j, \quad (4)$$

where  $C_i$  is the molar concentration of the  $i$ th species, and the expression of its change rate is given as

$$(\dot{C}_i)_j = (v_{ji}'' - v_{ji}) \left[ k_{f,j} \prod_{k=1}^{ns} (C_k)^{v_{jk}} - k_{b,j} \prod_{k=1}^{ns} (C_k)^{v_{jk}''} \right]. \quad (5)$$

The chemical reaction rates are based on Gupta et al.'s data [13], which are calculated by the Arrhenius curve fits on the reaction controlling temperature  $T_k$ . Under the thermodynamic nonequilibrium condition, it is necessary to establish a combination of the interaction between the vibrational energy relaxation process and the chemical reaction process for temperature control. Park expresses the controlling temperature of the dissociation reaction as a function of the local translational temperature and vibrational temperature [6], namely,

$$T_k = T^n T_v^{1-n}, \quad 0.5 \leq n \leq 0.7. \quad (6)$$

For exchange reactions, charge exchange reactions, and recombination ionization reactions, the controlling temperature is equal to the translational temperature, which equals the vibrational temperature for impact ionization reactions.

The energy exchange is mainly achieved by molecular collision. If other forms of energy exchange are ignored, only the vibrational energy change is considered, which is caused by the species generation term and energy transfer between the translational-rotational and vibrational-electronic modes. The Landau-Teller model is used to calculate the exchange energy [5], and the vibrational energy source term is given by

$$\begin{aligned} \dot{\omega}_v &= \sum_i \dot{\omega}_{v,i}, \\ \dot{\omega}_{v,i} &= \rho_i \frac{e_{v,i}(T) - e_{v,i}}{\tau_i} + e_{v,i} \dot{\omega}_i, \end{aligned} \quad (7)$$

where  $e_{v,i}(T)$  is the equilibrium vibration energy of the  $i$ th species, and  $\tau_i$  is the vibration relaxation characteristic time of the  $i$ th species, which is calculated by the Park-corrected Millikan and White semiempirical formula [5].

The viscosity coefficient and thermal conductivity for each gas species are obtained by Blottner's curve fits [14] and Eucken's relation [5], respectively. The viscosity coefficient and thermal conductivity of the mixed gas are obtained

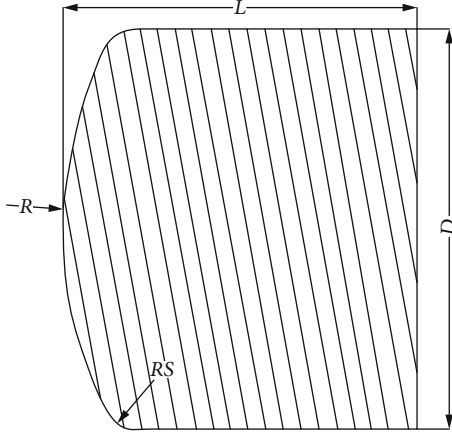


FIGURE 3: Schematic section of the blunt test model.



FIGURE 4: Blunt test model with sensors.

TABLE 1: Test parameters of the blunt model.

Run	Enthalpy (MJ/kg)	Total pressure in the chamber (MPa)	Total temperature in the chamber (K)
1	16.9	0.31	6482
2	18.0	0.50	6761

by Wilke's semiempirical mixing rule [15], and the mass diffusion coefficient for each species is calculated by the simplified formula assuming a constant Lewis number [11].

**2.2. Numerical Method.** The flow control equations in Section 2.1 are solved by the finite volume method based on the structural grid. The inviscid flux is calculated by the modified Steger-Warming scheme with MUSCL variable reconstruction [16, 17], while the viscous flux is calculated using the central difference scheme. The LU-SGS implicit method is

used for time iteration [18], and the convergence is accelerated by the local time step. The source term is calculated by the point implicit method, considering only the partial derivatives related to the species terms, and the Jacobian matrix of the source term is simplified by diagonalization.

At the nozzle inlet, the gas temperature and pressure are equal to the total temperature and total pressure in the chamber, respectively, the mass fraction of each species is obtained by thermodynamic equilibrium conditions, and then other parameters on the boundary are obtained through calculating the Riemann invariants [19, 20]. For the supersonic flow boundary, the parameters are determined by the free flow, and for the supersonic exit, the boundary parameters are extrapolated from the internal flowfield. The species mass fraction on the wall is calculated according to different catalytic boundaries. In order to improve the computational efficiency, the periodic boundary condition is used for axisymmetric flow [19]. There are two kinds of wall temperature boundaries, isothermal wall and radiation balance temperature boundary. In this paper, the wall temperature of the isothermal wall is taken as 300 K, while the other wall temperature is calculated by the following formula:

$$T_w = \left( \frac{q}{\varepsilon \sigma} \right)^{0.25}, \quad (8)$$

where  $q$  is the heat flux acting on the model surface,  $\varepsilon$  is the material emissivity (being 0.85 in this paper), and  $\sigma$  is the Stefan-Boltzmann constant equaling  $5.6703 \times 10^{-8} \text{ W}/(\text{m}^2 \cdot \text{K}^4)$ .

**2.3. Method Validation.** The numerical method is validated by flight data of the ELECTRE vehicle [12, 21] and test measurement data in the arc-heated wind tunnel [22].

The ELECTRE vehicle is a sphero-conical configuration with an overall length of 2 m, cone half-angle of 4.6 degrees, and nose radius of 0.175 m. One trajectory point is chosen with the free stream condition of altitude 53.3 km and Mach number 13 [21]. The fixed wall temperature of 343 K is assumed for the fully catalytic and noncatalytic wall boundary conditions. The normal spacing of the grid at the wall surface is  $10^{-5} \text{ m}$ , as the cell Reynolds number is on the order of one.

The flowfield parameters near the nose of the ELECTRE vehicle are shown in Figure 1. The translational temperature distribution shows in good agreement for the different catalytic boundary, but the difference of the oxygen atom mass fraction is obvious because of the different degree of recombination reaction. The predicted heat flux on the surface is compared with the flight data in Figure 2. Most of the flight data are lower than that of the fully catalytic boundary and higher than that of the noncatalytic boundary, which indicates that the surface material of the ELECTRE vehicle has partially catalytic properties. The reliability of the numerical method is validated for flight conditions, because of an error of 10% to 15% in the computation originating from the uncertainties in free stream conditions, thermocouple signal, etc. [21].



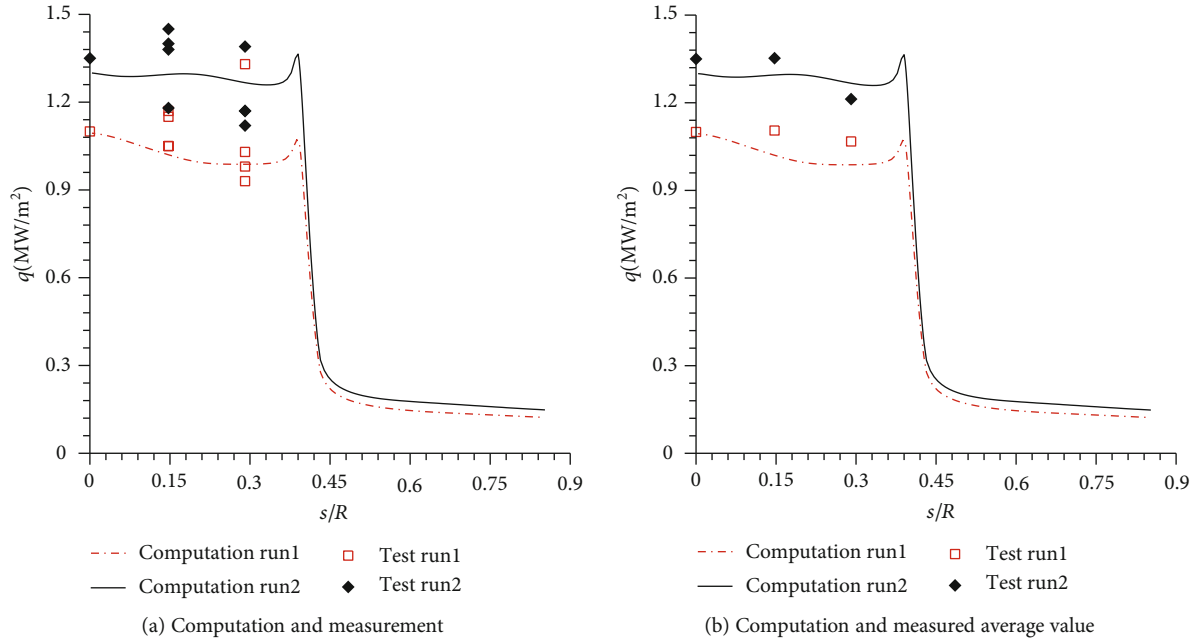


FIGURE 5: Heat flux along the surface of the blunt model.

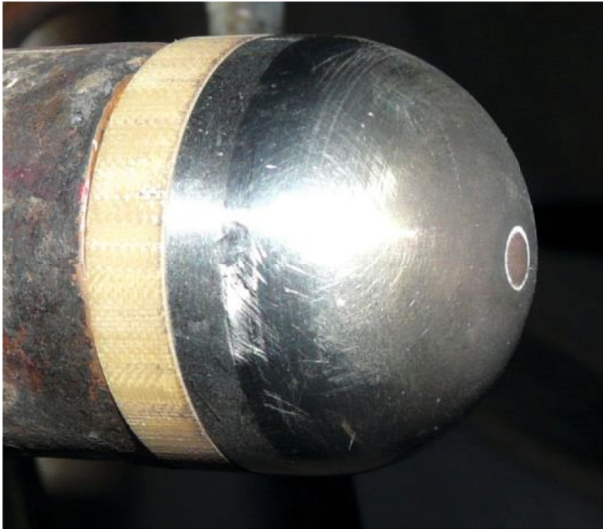


FIGURE 6: Spherical cylinder model.

The blunt test model is chosen to validate the numerical method, with a nose radius of 0.15 m, a shoulder radius of 0.005 m, an overall radius of 0.12 m, and a length of 0.08 m; its cross-section is shown in Figure 3. The surface heat flux is measured (Figure 4) in the arc-heated wind tunnel with the high enthalpy test conditions given in Table 1 [22].

The wall of the model is assumed to be fully catalytic with a fixed temperature of 300 K. The conical nozzle with a throat diameter of 0.03 m and an outlet diameter of 0.5 m is used in the test. Because of the large uniform flowfield at the nozzle exit, the internal flow in the nozzle and the flow around the model in the test section are calculated separately. This

TABLE 2: Flight and ground conditions under similar enthalpy and calibrated heat flux.

Enthalpy (MJ/kg)	Calibrated heat flux (MW/m <sup>2</sup> )	Flight altitude (km)	Flight speed (m/s)	Total temperature in the chamber (K)	Total pressure in the chamber (MPa)
10	4.0	48.0	4500	5200	1.02
10	5.0	45.0	4500	5268	1.50
10	6.0	43.0	4500	5321	2.00
10	7.0	41.0	4500	5370	2.60
16	4.0	60.0	5600	6473	0.45
16	5.0	56.0	5600	6625	0.75
16	6.0	53.0	5600	6678	0.90
16	7.0	51.0	5600	6766	1.20
20	4.0	65.0	6300	6802	0.30
20	5.0	62.5	6300	6963	0.48
20	6.0	60.0	6300	7096	0.70
20	7.0	57.5	6300	7167	0.85

method has no great influence on the flowfield or the thermal load on the model surface but can thus obviously improve the grid generation and calculation efficiency [22].

The heat flux on the surface of the blunt model is compared in Figure 5; it shows that the predicted heat flux is in good agreement with the measured data in the arc-heated wind tunnel [22]. Compared with the average value of test data, the error is lower than 10%. So, the numerical method for predicting the heat flux under test conditions has good reliability because the measurement error is about 15% from

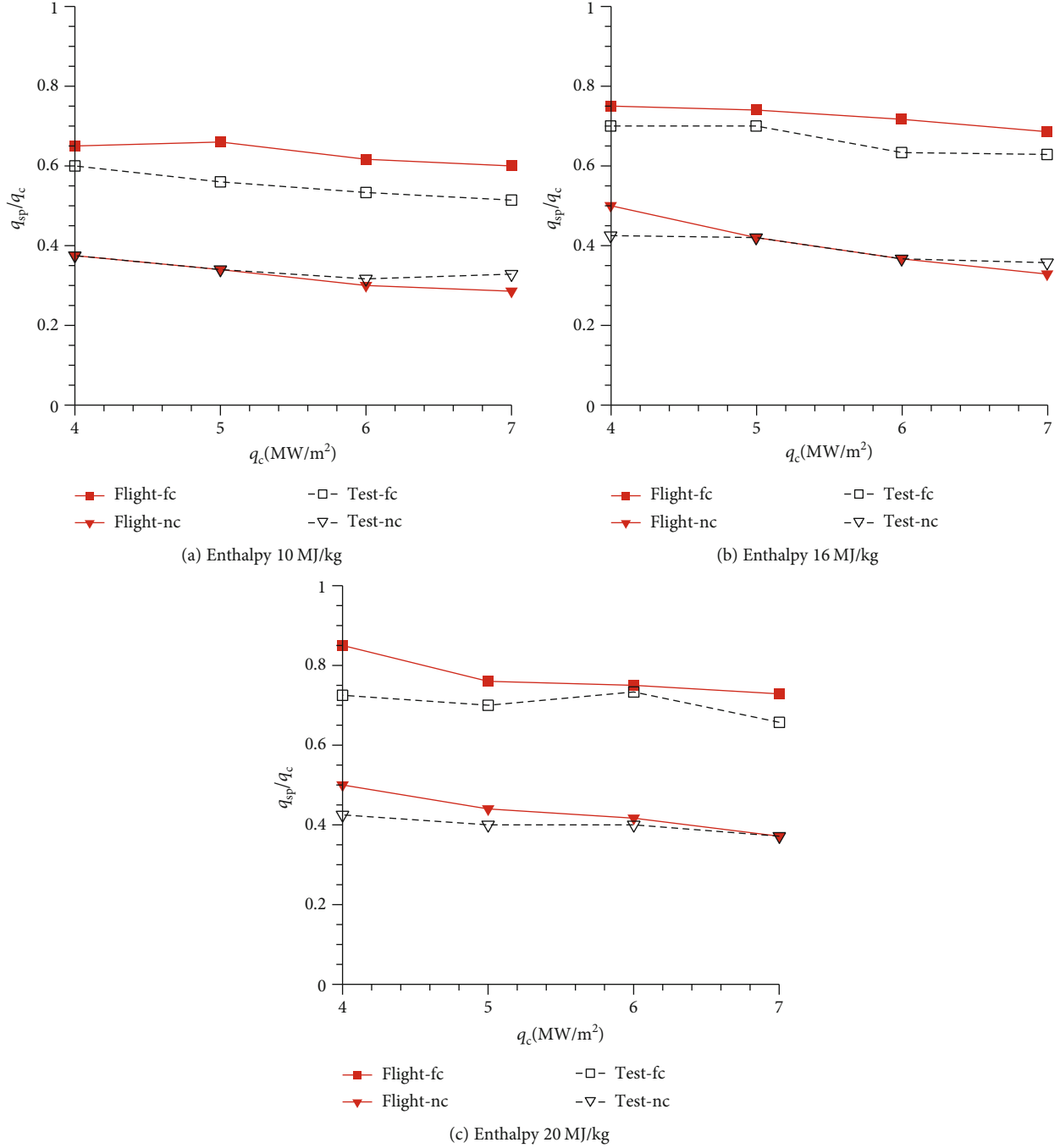


FIGURE 7: Comparison of the stagnation point heat flux with the radiation balance boundary.

the uncertainties in flowfield repeatability, sensor fabrication and installation, test system, etc. [23].

### 3. Results and Discussion

**3.1. Difference of Heat Flux.** In this paper, the test simulation method is investigated for a spherical cylinder model with a nose radius of 0.035 m and a length of 0.05 m (Figure 6); the conical nozzle with a throat diameter of 0.03 m and an outlet diameter of 0.2 m is used. Different enthalpy (10 MJ/kg, 16 MJ/kg, and 20 MJ/kg) and different calibrated heat flux (4 MW/m<sup>2</sup>, 5 MW/m<sup>2</sup>, 6 MW/m<sup>2</sup>, and 7 MW/m<sup>2</sup>)

with the fully catalytic wall boundary and fixed wall temperature of 300 K are preset. The flight and ground test conditions for set enthalpy and calibrated heat flux are obtained by numerical simulation of many conditions, which are listed in Table 2. For the flight conditions, enthalpy is mainly related to flight velocity, and the calibrated heat flux increases with the decrease of flight altitude under certain enthalpy. For the ground test conditions in the arc-heated wind tunnel, the calibrated heat flux increases with the increase of total pressure in the chamber.

For the flight and ground test conditions, the wall temperature boundary of the model is changed from the

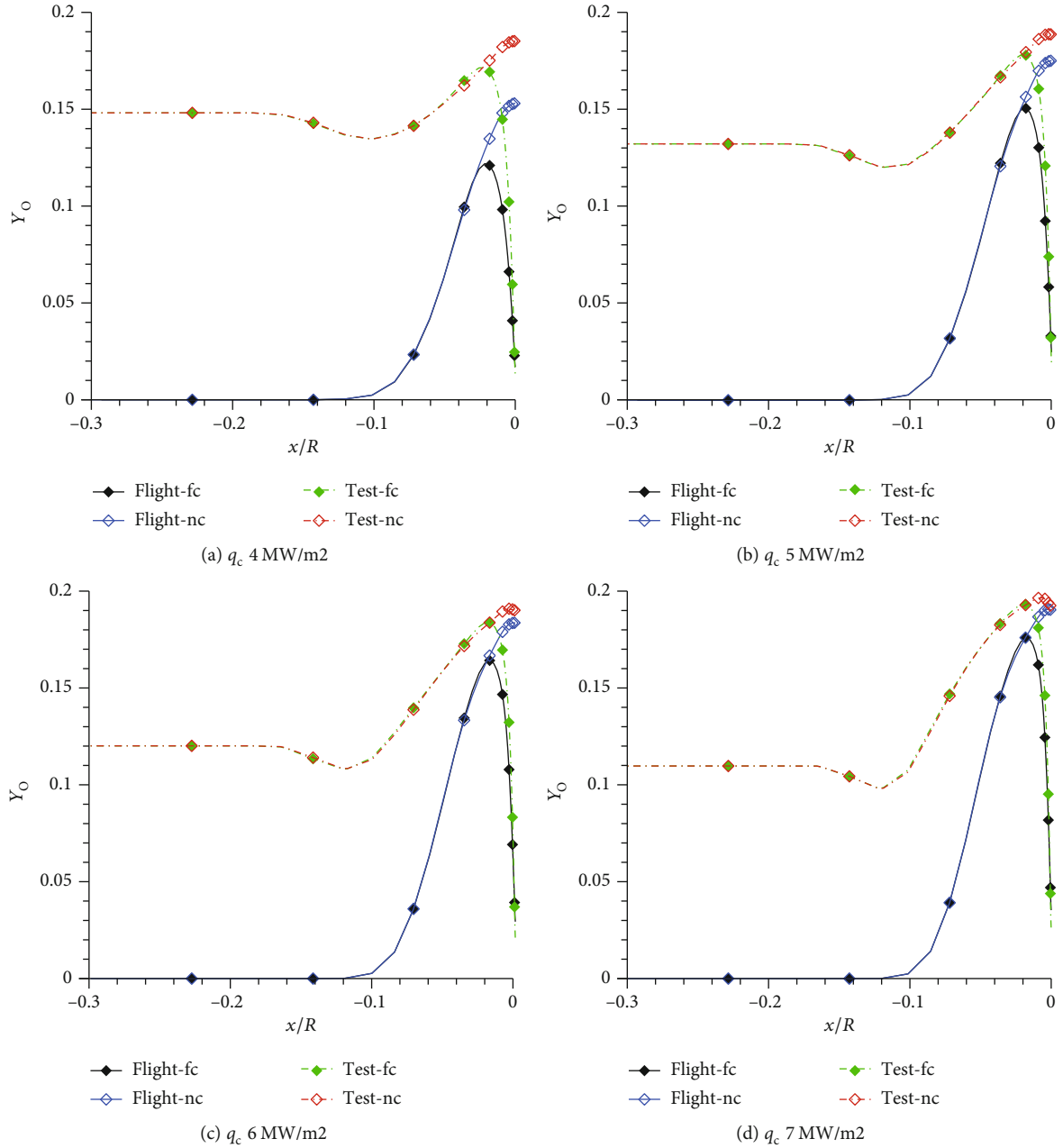


FIGURE 8: Comparison of oxygen atom mass fractions on the stagnation line for enthalpy 10 MJ/kg.

isothermal wall to the radiation balance temperature boundary. The high enthalpy flowfield with the fully catalytic and noncatalytic walls is simulated, and the heat flux on the stagnation point is compared in this section.

In this paper,  $q_c$  is the calibrated heat flux, and  $q_{sp}$  is the stagnation point heat flux on the modified wall boundary. The symbols “fc” and “nc” stand for the fully catalytic and noncatalytic walls, respectively. It can be seen from the comparison in Figure 7 that when the radiation balance temperature boundary is adopted on the wall, the stagnation point heat flux under the flight and ground test conditions decreases compared with that using the isothermal wall boundary. The slopes of the curves in Figure 7 are almost

all negative, and they are close to each other; this shows that the change of stagnation point heat flux is more obvious under the conditions with higher calibrated heat flux.

Under the flight conditions, the stagnation point heat flux drops to about 60% to 85% of the calibrated heat flux for the fully catalytic wall and about 30% to 50% for the noncatalytic wall. Under the ground test conditions, the stagnation point heat flux is about 50% to 80% of the calibrated heat flux for the fully catalytic wall and about 40% for the noncatalytic wall.

For the fully catalytic boundary, the stagnation point heat flux in the flight conditions is higher than that in the corresponding ground test conditions. For the cold wall boundary,

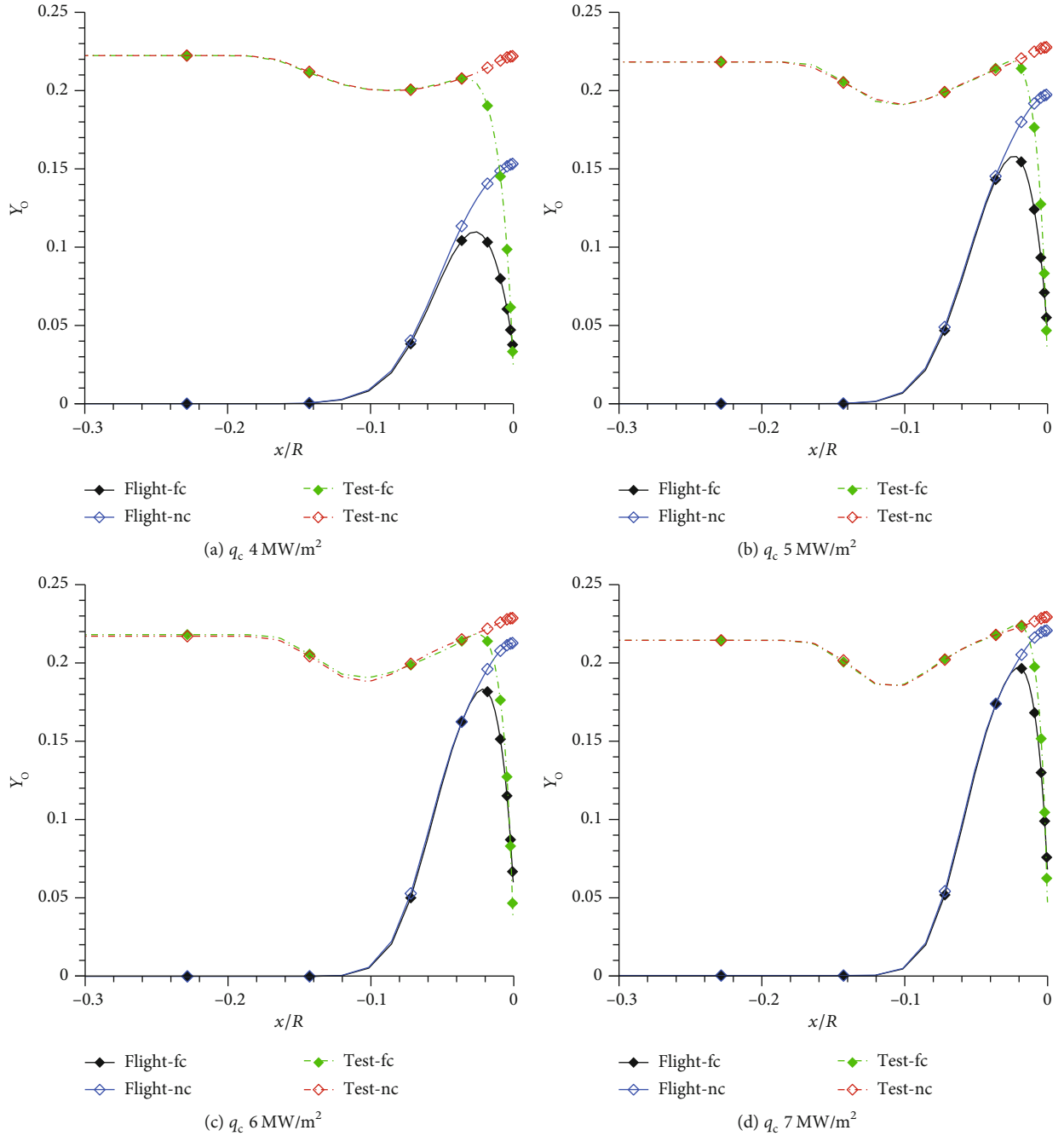


FIGURE 9: Comparison of oxygen atom mass fractions on the stagnation line for enthalpy 16 MJ/kg.

because the recombination reaction produces more heat, the proportion of diffusion heat flux in calibrated heat flux under the test conditions is larger than that under the flight conditions. When the radiation balance temperature boundary is adopted, the change of diffusion heat flux in the test conditions caused by the surface recombination reaction is larger than that in the flight conditions. For the noncatalytic boundary, under the conditions of low enthalpy, the difference between the flight and ground test conditions in the cases of the low calibrated heat flux state is smaller than that of the high calibrated heat flux state (Figure 7(a)), while

under the conditions of high enthalpy, the difference in the high calibrated heat flux state is smaller than that in the low calibrated heat flux state (Figure 7(c)). However, it can be seen that the overall difference is small for the noncatalytic boundary, less than 10% for most conditions. The results show that the effectiveness of the simulated heat flux is different for materials with different catalytic characteristics.

In order to achieve the best assessment effect for surface heat flux, the test operating parameters of the ground wind tunnel need to be adjusted according to the material catalytic characteristics. For the fully catalytic material, the calibrated



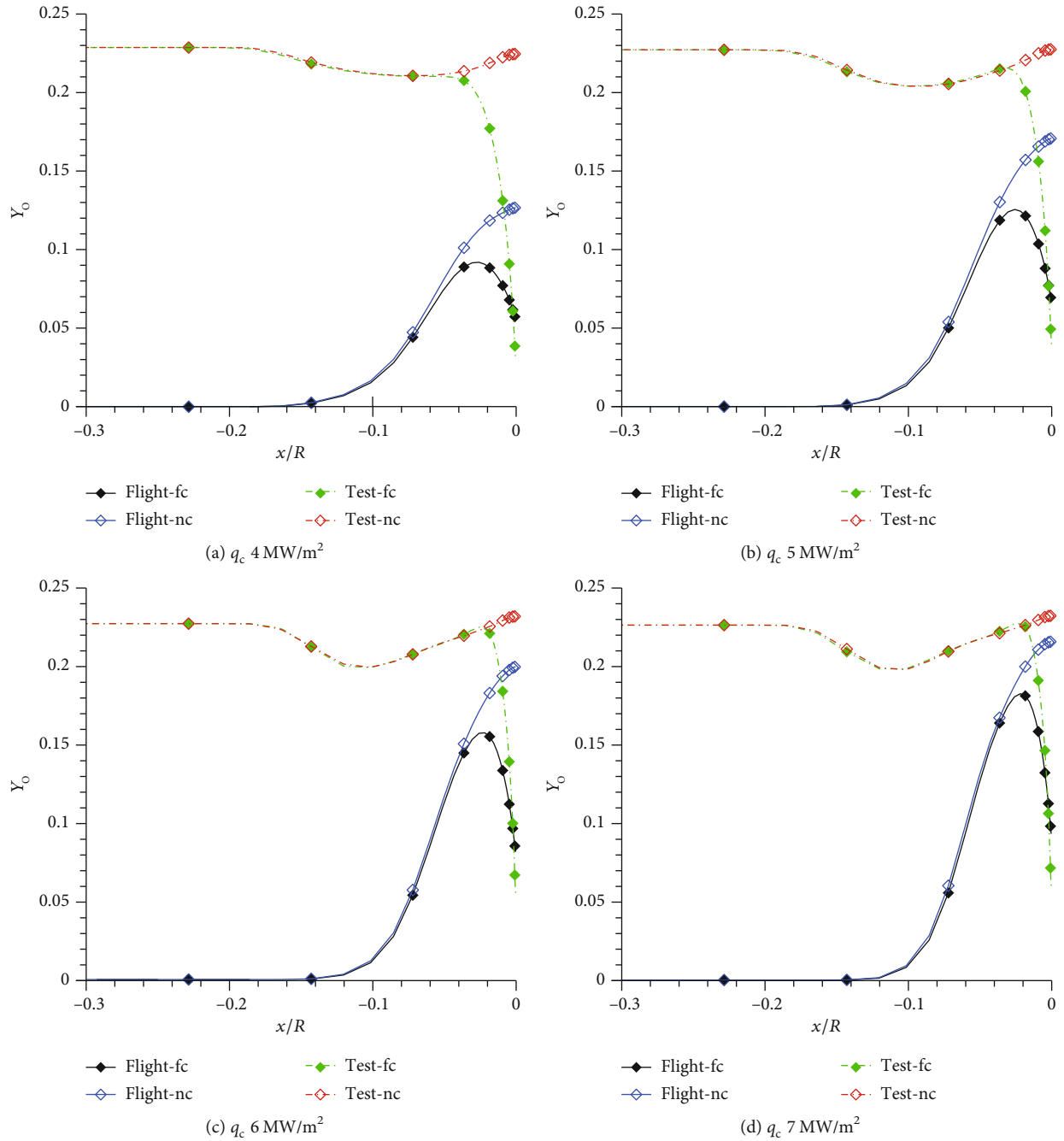


FIGURE 10: Comparison of oxygen atom mass fractions on the stagnation line for enthalpy 20 MJ/kg.

heat flux of the wind tunnel test should be higher than that of the corresponding flight condition, so the enthalpy or chamber total pressure in the test needs to be increased.

**3.2. Difference of the Oxygen Atom Mass Fraction.** The oxygen atom mass fraction near the wall may play a key role in the oxidative damage of the thermal protection material. Figures 8–10 show their distribution on the stagnation line of the flowfield in both the flight and ground test conditions.

Under the conditions of low enthalpy, the mass fraction of the oxygen atom in test incoming flow decreases with the increase of calibrated heat flux (Figure 8); this is due to the

fact that the dissociation of oxygen molecules is inhibited to some extent by high total pressure. Under the conditions of high enthalpy, there is little difference in test incoming flow because the oxygen molecules dissociate completely (Figures 9 and 10).

For the fully catalytic wall boundary, the mass fraction of the oxygen atom after the shock wave is decreased significantly from a peak value due to the recombination reaction near the surface. However, for the noncatalytic wall boundary, its change is not obvious along the normal direction from the shock wave to the surface of the model, because there is no recombination reaction near the wall surface.

TABLE 3: The peak mass fraction of the oxygen atom after the shock wave.

Enthalpy (MJ/kg)	Calibrated heat flux (MW/m <sup>2</sup> )	Flight with the fully catalytic boundary	Test with the fully catalytic boundary	Difference for the fully catalytic boundary	Flight with the noncatalytic boundary	Test with the noncatalytic boundary	Difference for the noncatalytic boundary
10	4.0	0.122	0.171	0.049	0.153	0.185	0.032
10	5.0	0.150	0.178	0.028	0.175	0.189	0.014
10	6.0	0.164	0.184	0.020	0.184	0.191	0.007
10	7.0	0.176	0.193	0.017	0.191	0.197	0.006
16	4.0	0.110	0.208	0.098	0.153	0.222	0.069
16	5.0	0.158	0.217	0.059	0.197	0.228	0.031
16	6.0	0.183	0.218	0.035	0.213	0.229	0.016
16	7.0	0.196	0.223	0.027	0.220	0.229	0.009
20	4.0	0.092	0.207	0.115	0.127	0.225	0.098
20	5.0	0.125	0.216	0.091	0.171	0.227	0.056
20	6.0	0.157	0.224	0.067	0.199	0.231	0.032
20	7.0	0.182	0.227	0.045	0.215	0.232	0.017

TABLE 4: The conditions under similar stagnation point heat flux and oxygen atom mass fraction after the shock wave.

Enthalpy of flight conditions (MJ/kg)	Calibrated heat flux (MW/m <sup>2</sup> )	Stagnation point heat flux (MW/m <sup>2</sup> )	Oxygen atom mass fraction after the shock wave	Enthalpy of test conditions (MJ/kg)	Total pressure of test conditions (MPa)
10	4.0	1.7	0.14	8.0	2.2
10	5.0	1.9	0.17	9.0	2.0
10	6.0	2.0	0.18	10.0	1.9
10	7.0	2.1	0.19	10.0	2.2
16	4.0	2.2	0.13	8.0	3.7
16	5.0	2.4	0.18	9.5	3.0
16	6.0	2.6	0.20	10.5	2.8
16	7.0	2.7	0.21	11.0	3.0
20	4.0	2.9	0.11	—	—
20	5.0	3.0	0.15	—	—
20	6.0	3.1	0.18	9.0	5.0
20	7.0	3.2	0.20	10.5	4.1

Under the conditions of similar enthalpy, with the increase of the calibrated heat flux, the difference peak mass fraction of the oxygen atom after the shock wave between the flight and ground test conditions becomes smaller. For the test conditions, the peak value changes with calibrated heat flux are very small. However, for the flight conditions with higher calibrated heat flux, because of the lower altitude or higher air density, the collision between the gas molecules is vigorous and the dissociation is more sufficient after the shock wave, which makes the mass fraction of the oxygen atom after the shock wave larger and closer than that of the corresponding test condition. This difference is shown in Table 3.

It can be seen from these figures and Table 3 that the mass fraction of the oxygen atom after the shock wave in flight conditions is generally lower than that in the corresponding test conditions. In particular, the difference is more obvious with the fully catalytic boundary. Therefore, if it is necessary to pay attention to the oxidation resistance of the material, the original test simulation method cannot meet

the requirement of the oxygen atom mass fraction near the wall and must be adjusted to accomplish the assessment object, such as reducing the enthalpy in the wind tunnel test.

*3.3. Test Simulation Method for Partially Catalytic Material.* It is necessary to explore the possibility of simulating the surface heat flux and the oxygen atom mass fraction after the shock wave in the arc-heated wind tunnel test. The partially catalytic boundary is used for the model wall; the material catalytic coefficient is obtained by

$$\gamma = \frac{0.3303}{p_A} \exp\left(\frac{-13105}{T_w}\right), \quad (9)$$

where  $p_A$  is the atomic partial pressure and  $T_w$  is the wall temperature [24].

The test conditions are given in Table 4 under similar stagnation point heat flux and oxygen atom mass fraction after the shock wave for the partially catalytic material and

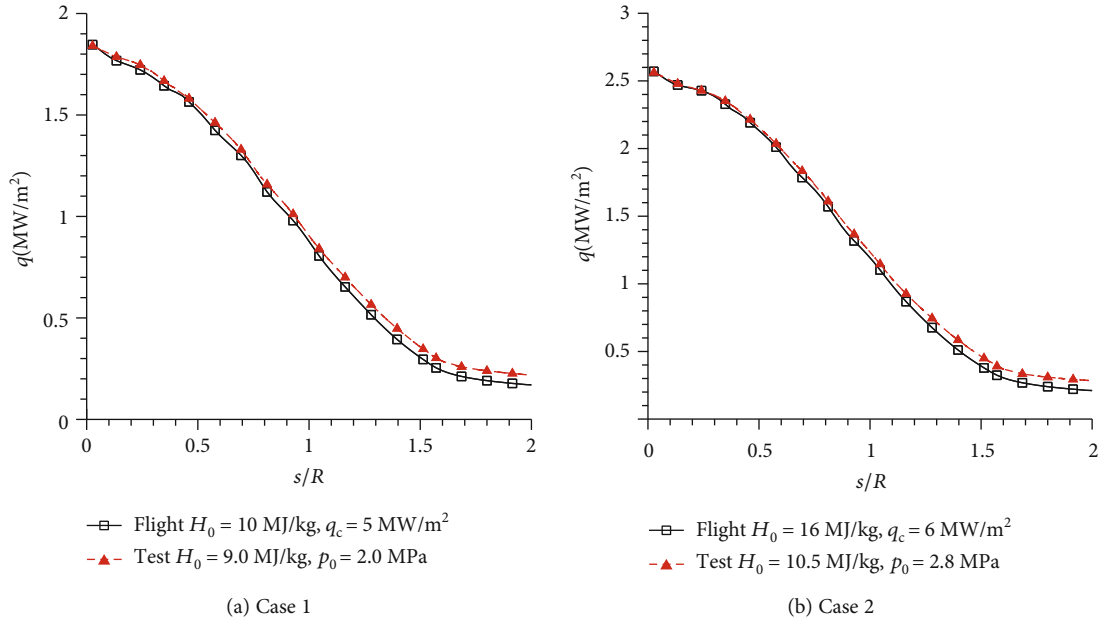


FIGURE 11: Comparison of the surface heat flux on the center line.

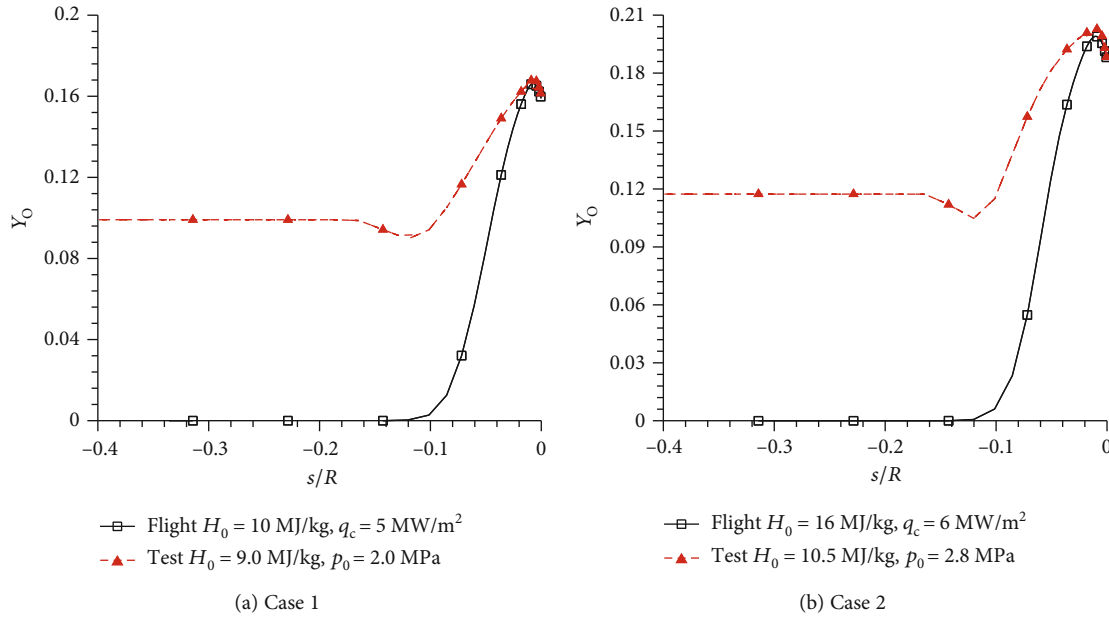


FIGURE 12: Comparison of the oxygen atom mass fraction on the stagnation line.

radiation balance temperature boundary, in which some conditions of the enthalpy 20 MJ/kg have obviously exceeded the test facility power of the 20 MW arc-heated wind tunnel. In order to achieve the simulation goal, the enthalpy of the arc-heated wind tunnel test needs to be adjusted and is no longer equal to the enthalpy of the corresponding flight conditions for most cases. For the low enthalpy of the flight conditions, the enthalpy adjustment range is small, while for the high enthalpy of the flight conditions, the adjustment range is large. Meanwhile, it is necessary to adjust the chamber total pressure in the ground test to ensure the surface heat flux is similar to that of the flight condition.

Figures 11 and 12 show the comparison of the surface heat flux and the oxygen atom mass fraction on the stagnation line, respectively, for two cases in Table 4. The pressure and oxygen atom mass fraction on the symmetry plane of the two cases are compared, respectively, in Figures 13 and 14. Although the oxygen atom mass fraction in the free stream of the ground test is much larger than that of the corresponding flight condition, there is no significant difference near the wall surface. This conclusion is of great significance for simulating the thermochemical nonequilibrium effect in the high enthalpy flowfield. Moreover, it can be seen that the ground wind tunnel test cannot simulate all the parameters of the

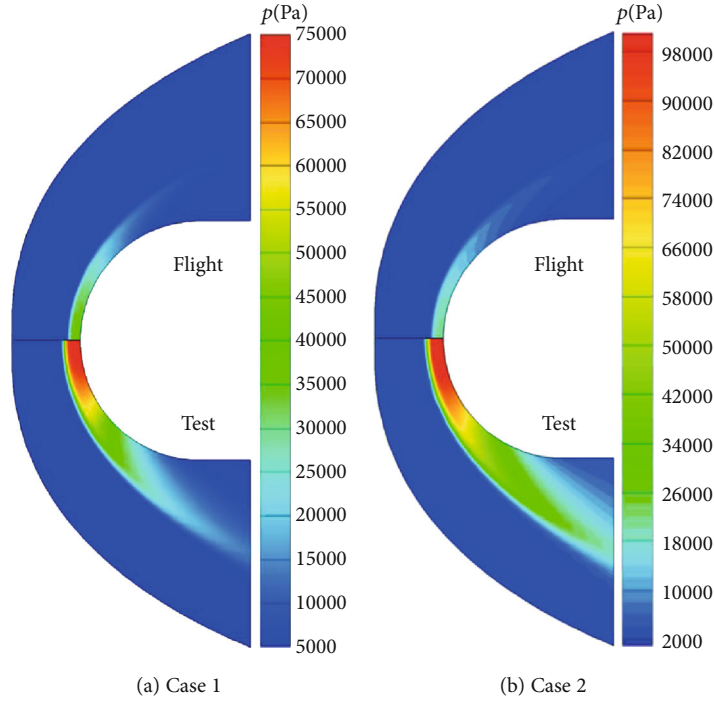


FIGURE 13: Comparison of the pressure on the symmetric plane.

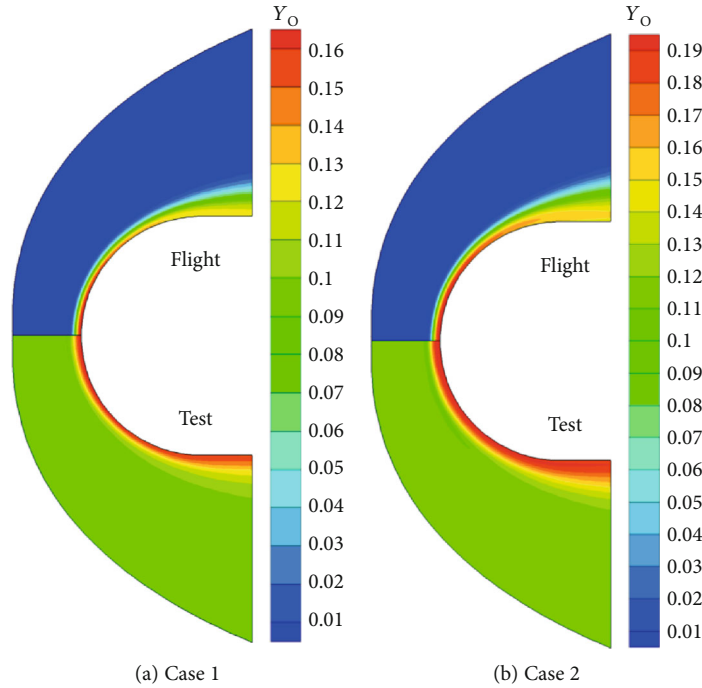


FIGURE 14: Comparison of the oxygen atom mass fraction on the symmetric plane.

flight conditions, such as the enthalpy, stagnation point heat flux, surface pressure, and oxygen atom mass fraction after the shock wave. In the wind tunnel test, when the heat flux and the oxygen atom mass fraction are simulated by adjusting the enthalpy, the difference of pressure after the shock wave increases reluctantly. Hence, it is necessary to adjust the test operation conditions according to the concerned parameters to better simulate the flight conditions and

achieve the purpose of assessment for the ground wind tunnel test.

#### 4. Conclusions

This study shows that numerical simulation can assist the test design to improve the effectiveness of the thermal assessment test, and the test simulation method of the arc-heated wind

tunnel can be improved for different parameters. The comparative analysis of the high enthalpy flowfield around a spherical cylinder reveals the following findings:

- (1) Under the free stream conditions with similar enthalpy and calibrated heat flux, the stagnation point heat flux on the fully catalytic wall in the ground test conditions is lower than that in the corresponding flight conditions with the radiation balance temperature boundary. This shows that the test simulation method cannot assess the heat flux on the model surface. However, for the noncatalytic wall, the difference between the flight and ground test conditions is negligible
- (2) With similar enthalpy and calibrated heat flux, the oxygen atom mass fraction after the shock wave in the flight conditions is generally lower than the oxygen atom mass fraction under the corresponding ground test condition, resulting in a different gradient near the wall surface. In this case, the ground test cannot properly simulate the oxidative damage of the thermal protection material
- (3) To simulate the surface heat flux and the oxygen atom mass fraction near the wall of the flight conditions, it is necessary to reduce the enthalpy or increase the total pressure in the arc-heated wind tunnel test

## Data Availability

The data used to support the findings of this study are included within the article.

## Conflicts of Interest

The authors declare that there is no conflict of interests regarding the publication of this paper.

## Acknowledgments

This work is supported by the National Natural Science Foundation of China (Grant no. 91641201).

## References

- [1] J. Sheeley, "Arc heated wind tunnel failure prediction using artificial neural networks," in *43rd AIAA Aerospace Sciences Meeting and Exhibit*, Reno, Nevada, USA, January 2005.
- [2] I. Terrazas-Salinas, J. E. Carballo, D. M. Driver, and J. Balboni, "Comparison of heat transfer measurement devices in arc jet flows with shear," in *10th AIAA/ASME Joint Thermophysics and Heat Transfer Conference*, Chicago, Illinois, USA, June 2010.
- [3] C. S. Nie, Y. Li, J. D. Huang, and W. B. Miao, "Test of aero-heating in hypersonic non-equilibrium flow and numerical simulation study," *Scientia Sinica Technologica*, vol. 48, no. 8, pp. 845–852, 2018.
- [4] M. S. Ding, W. Z. Dong, T. S. Gao, T. Jiang, and Q. Z. Liu, "Computational analysis of the local catalytic property distinction influence on aero-thermal environments," *Acta Aeronautica et Astronautica Sinica (Chinese Journal)*, vol. 39, no. 3, article 121588, 2018.
- [5] G. V. Candler, "The computation of weakly ionized hypersonic flows in thermo-chemical nonequilibrium, [PhD thesis]," Stanford University, 1988.
- [6] C. Park, *Nonequilibrium Hypersonic Aerothermo-Dynamics*, John Wiley and Sons, New York, 1990.
- [7] A. Anna and I. D. Boyd, "Numerical analysis of surface chemistry in high-enthalpy flows," *Journal of Thermophysics and Heat Transfer*, vol. 29, no. 4, pp. 653–670, 2015.
- [8] T. Gökçen, J. Balboni, and A. I. Alunni, "Computational simulations of the 10-MW TP3 arc-jet facility flow," in *45th AIAA Thermophysics Conference*, Dallas, Texas, USA, June 2015.
- [9] M. P. Loomis, F. Hui, S. Polsky, E. Venkatapathy, and D. Prabhu, "Arc-jet semi-elliptic nozzle simulations and validation in support of X-33 TPS testing," in *36th AIAA Aerospace Sciences Meeting and Exhibit*, Reno, Nevada, USA, January 1998.
- [10] J. H. Grinstead, D. A. Stewart, and C. A. Smith, "High enthalpy test methodologies for thermal protection systems development at NASA Ames Research Center," in *AIAA/CIRA 13th International Space Planes and Hypersonics Systems and Technologies Conference*, Capua, Italy, May 2005.
- [11] L. C. Scalabrin, "Numerical simulation of weakly ionized hypersonic flow over reentry capsules, [PhD thesis]," University of Michigan, 2007.
- [12] J. Hao, J. Wang, and C. Lee, "Numerical study of hypersonic flows over reentry configurations with different chemical non-equilibrium models," *Acta Astronautica*, vol. 126, pp. 1–10, 2016.
- [13] R. N. Gupta, J. M. Yos, and R. A. Thompson, "A review of reaction rates and thermodynamic and transport properties for the 11-species air model for chemical and thermal nonequilibrium calculations to 30000K," *NASA Technical Memorandum*, vol. 101528, 1989.
- [14] F. G. Blottner, M. Johnson, and M. Ellis, "Chemically reacting viscous flow program for multi-component gas mixtures," Sandia Laboratories, Albuquerque, New Mexico, 1971, SC-RR-70-754.
- [15] C. R. Wilke, "A viscosity equation for gas mixtures," *Journal of Chemical Physics*, vol. 18, no. 4, pp. 517–519, 1950.
- [16] J. L. Steger and R. F. Warming, "Flux vector splitting of the inviscid gasdynamic equations with application to finite-difference methods," *Journal of Computational Physics*, vol. 40, no. 2, pp. 263–293, 1981.
- [17] R. W. MacCormack and G. V. Candler, "The solution of the Navier-Stokes equations using Gauss-Seidel line relaxation," *Computers & Fluids*, vol. 17, no. 1, pp. 135–150, 1989.
- [18] S. Yoon and A. Jameson, "Lower-upper symmetric-Gauss-Seidel method for the Euler and Navier-Stokes equations," *AIAA Journal*, vol. 26, no. 9, pp. 1025–1026, 1988.
- [19] S. L. Krist, R. T. Biedron, and C. L. Rumsey, *CFL 3D User's Manual (Version 5.0)*, NASA/TM-1998-208444, 1998.
- [20] A. Mazaheri, "Multispecies reacting characteristic boundary condition implementation with applications," *Journal of Spacecraft and Rockets*, vol. 50, no. 2, pp. 467–470, 2013.
- [21] J. Muylaert, L. Walpot, J. Häuser et al., "Standard model testing in the European high enthalpy facility F4 and extrapolation to flight," in *AIAA 17th Aerospace Ground Testing Conference*, Nashville, TN, USA, July 1992.



- [22] W. Q. Luo, J. H. Liang, Y. J. Yang, H. H. Sun, and J. S. Zhao, "Study on high enthalpy flowfield simulation and aerothermal verification in the arc-heated wind tunnel," *Journal of Propulsion Technology (Chinese Journal)*, vol. 41, no. 4, pp. 916–924, 2020.
- [23] L. Zeng, "Study on data processing method and error mechanism analysis of heat flux measurement in wind tunnel, [PhD thesis]," China Aerodynamics Research and Development Center, 2012.
- [24] L. P. Liu, G. L. Wang, Y. G. Wang, H. J. Ma, J. Luo, and J. Zhang, "Test methods for determining surface catalytic properties of thermal protection materials in high enthalpy chemical non-equilibrium flows," *Acta Aeronautica et Astronautica Sinica (Chinese Journal)*, vol. 38, no. 10, article 121317, 2017.